

## Research Article

# Design and Bulk Sensitivity Analysis of a Silicon Nitride Photonic Biosensor for Cancer Cell Detection

Prasanna Kumar S.  and Sivabramanian A. 

*School of Electronics Engineering, Vellore Institute of Technology, Chennai 600127, India*

Correspondence should be addressed to Sivabramanian A.; [sivasubramanian.a@vit.ac.in](mailto:sivasubramanian.a@vit.ac.in)

Received 19 January 2022; Revised 24 March 2022; Accepted 11 April 2022; Published 25 May 2022

Academic Editor: Bhagwan Das

Copyright © 2022 Prasanna Kumar S. and Sivabramanian A.. This is an open access article distributed under the Creative Commons Attribution License, which permits unrestricted use, distribution, and reproduction in any medium, provided the original work is properly cited.

Bulk sensitivity is an important parameter to validate the efficiency of the photonic waveguide sensor. Due to recent advancements in point-of-care silicon photonic biosensing, the focus is to identify the effective way to improve sensitivity. Integrating polydimethylsiloxane (PDMS) microfluidic channel in sensor architecture decreases the sensitivity due to leakage of molecules at edges. The silicon nitride (SiN<sub>4</sub>) Mach-Zehnder interferometer utilizes the refractive index of different cancer cells (1.39–1.401) to determine the bulk sensitivity. The proposed gradient step rib-slot structure of 970 nm wide and 400 nm thickness is designed to hold the liquid sample without any PDMS material. This novel waveguide exhibits high waveguide bulk sensitivity  $S_{w,bulk}$  and device bulk sensitivity  $S_d$  compared with the gradient rib waveguide. We achieved a waveguide bulk sensitivity ( $S_{w,bulk}$ ) of 2.0699 RIU/RIU and device sensitivity ( $S_d$ ) of 568 nm/RIU through finite-difference time-domain (FDTD) analysis.

## 1. Introduction

Virus has been a significant outbreak in recent times. Interest in label-free biosensors has increased due to the diagnosis techniques used in postpandemic [1]. Cancer is the most severe disease globally at present [2]. There are more than 100 different types of cancer group cells that will affect every organ in a body [3]. Early detection of cancer in postpandemic is most important in current diagnosis and medication techniques [4]. Due to its rapid detection and high sensitivity capability, low-cost label-free point-of-care biosensors are developed [5]. Many research findings were reported in the literature on detection of target molecules in biological and environmental applications [6, 7]. Biosensors can be classified based on transduction mechanisms such as electrochemical, electro-optical, optical, mechanical, acoustical, chemical-immunoassays, spectroscopy [8], and image processing algorithms [9, 10]. In an optical method, no-chemical reagents are added to the sample [11]. This will increase the sensitivity to quantify the biomolecule present in the sample [12]. In future, the point-of-care devices may be integrated with mobile phones [13]. By considering all

these parameters, we chose a silicon photonic waveguide biosensor [14].

This silicon-based photonic device can be easily fabricated using the available CMOS foundry. This platform offers a wide variety of optimization based on application. The optimization may be waveguide geometry, spectrum analyzer, CCD (charge coupled device) detector, light sources, etc. [15]. For cancer cell detection, the main challenges are absorption of a biomolecule into the waveguide [16]. Integrating polydimethylsiloxane (PDMS) microfluidic channel in sensor architecture decreases the sensitivity due to leakage of molecules at edges. Silicon nitride waveguides are preferred as they offer low waveguide loss and are flexible in fabrication compared with silicon-on-insulator (SOI) waveguides [17, 18]. Some recent reports on fabrication up to 900 nm thickness are done without any cracking stress on silicon nitride [19]. Mach-Zehnder interferometer (MZI) exhibits good response for the cancer blood cell as MZI sensing arm has long length interaction over the sample, and dynamic waveguide structures are integrated [20].

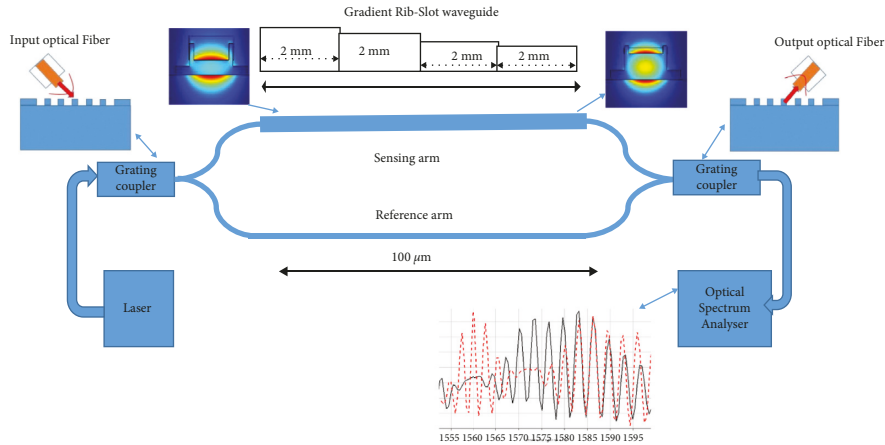


FIGURE 1: Silicon nitride biosensor setup with MZI and a grating coupler.

In this article, we analyzed the silicon nitride MZI sensor architecture for cancer cell detection using gradient rib and gradient rib-slot waveguide, as shown in Figure 1 [18, 21]. We use cancer cell blood samples as bulk solution for sensing. For bulk sensitivity, the interferometer-based sensor offers a high sensitivity in the range of 10<sup>-7</sup> to 10<sup>-8</sup> RIU [22]. By integrating the polydimethylsiloxane (PDMS) microfluidic channel in the sensor, architecture decreases the waveguide bulk sensitivity ( $S_{w,bulk}$ ) and device sensitivity ( $S_d$ ) due to leakage of molecules at edges [23]. As evanescent field decays linearly over the length of the waveguide and to avoid antibody diffusion on the surface, we propose gradient step for every 2 mm length. The response of the gradient rib waveguide over the normal cell and cancer cell in the transmission spectrum is minimal, and  $S_{w,bulk}$  is 0.2568 RIU/RIU.

Our objective of the design is to accommodate analytes in the photonic biosensor integrated to mobile phones, which would increase the detection rate and sensitivity; hence, we proposed the design of a novel gradient rib-slot waveguide of rib width 970 nm, slot width 790 nm, and thickness 400 nm. This optimized structure holds the analyte without any external PDMS material and allows the sensor to be integrated with mobile phones in future. This structure also enhances the analyte transportation more effective. This results in increased interaction of analytes with light and exhibits more number of peaks in the transmission spectrum compared with the gradient-rib waveguide. The waveguide bulk sensitivity ( $S_{w,bulk}$ ) and device sensitivity ( $S_d$ ) were found to be 2.0699 RIU/RIU and 568 nm/RIU through finite-difference time-domain (FDTD) analysis. These results were obtained for cancer cells, and this approach may be extended to other generic biomolecules of different sizes and refractive indices.

## 2. Materials and Methods

In this section, basic components of the photonic waveguide biosensor and properties of MZI with two different types of waveguide geometry structures are presented.

**2.1. Properties of the Proposed Silicon Nitride (Si<sub>3</sub>N<sub>4</sub>) Photonic Waveguide Biosensor.** Silicon nitride offers broad biosensing applications for integrated point-of-care devices. The operating wavelength of silicon nitride ranges from 400 nm to 3.7 μm [18], which provides scope for designing instant-sensing biophotonic chip that can be integrated to mobile phones in future. In the asymmetric Mach-Zehnder interferometer configuration, the rib and novel rib-slot waveguide are used as the sensing arm. The other waveguide sensing structures are strip [24, 25], slot [26], double-slot [27], and sub-wavelength grating [28, 29] for biosensing applications to detect various diseases. The interferometer sensor gives high sensitivity (10<sup>-7</sup> to 10<sup>-8</sup> RIU), and it can operate at a telecommunication wavelength. Optimization of MZI improves the sensitivity of the sensor based on the evanescent field absorption over the waveguide structure. The design of the waveguide structure is different depending on the concentration of the sample used [30]. To increase the interaction of the evanescent field over the sensing arm, the proposed design of the novel gradient rib-slot waveguide structure has a sensing window of length 8 mm with an analyte volume of  $1.0476 \times 10^{-6} \text{ mm}^3$ . In FDTD simulation, each gradient step length of 2 mm has different analyte thicknesses ranging from 400 nm to 90 nm. Our earlier study [31] showed that the sensitivity of the silicon nitride waveguide structure is better than the silicon waveguide structure. Better absorption in the transmission spectrum leads to detect a particular biomolecule present in the sample. The transmission loss in the waveguide depends on the absorption of photons by the sample in the cladding region. In most commonly used 450 nm width wire waveguide, the loss ranges from 2.5 dB to 3.5 dB. The roughness of the sidewalls can significantly influence the propagation loss. In addition, when the rib waveguide is immersed in water, the intrinsic loss will decrease. Thus, the confinement factor of the rib waveguide is smaller, but it is more tolerant to fabrication process errors due to waveguide width variation. Sidewall roughness in the wire waveguide is vital for evanescent sensing. Rib waveguides are preferred for evanescent sensing because sidewall roughness has less effect on them [16].

**2.2. Analysis for Cancer Cell Detection.** Every disease blood cell sample has a different range in refractive index, and the blood sample of a healthy person is 1.35 [32].

The light propagation in MZI waveguide will be varied due to the refractive index of cancer cells with the analyte thickness of 400 nm, 250 nm, 150 nm, and 90 nm. In the waveguide simulation, the refractive index of the cancer cells is applied over the surface of the sensing arm of MZI [22], and the corresponding variation in the transmission spectrum of cancer cell and healthy blood sample at 1550 nm is observed by using Optical Spectrum Analyzer.

**2.3. Sensor Performance Evaluation by Sensitivity.** FDTD accurately simulates the physical activity of photonics and optoelectronic circuits and systems. Analysis of electromagnetic wave propagation in the photonic device was performed by the FDTD approach. Due to this, computational electromagnetics has become an important area of research in developing efficient sensing platforms. In the waveguide structure, the mode profile overlaps with analytes highly. The change in effective index ( $n_{\text{eff}}$ ) and refractive index of analyte ( $n_c$ ) can be in measurable quantity as bulk sensitivity [33].

The waveguide bulk sensitivity novel gradient strip-slot waveguide equation is as follows:

$$S_{w,\text{bulk}} = \frac{\partial n_{\text{eff}}}{\partial n_c} \frac{\text{RIU}}{\text{RIU}}. \quad (1)$$

Architecture (MZI) bulk sensitivity  $S_{a(\text{MZI}),\text{bulk}}$  equation for the novel gradient strip-slot waveguide with ( $\lambda_r$ ) shift in resonance wavelength is as follows:

$$S_{a(\text{MZI}),\text{bulk}} = \frac{\partial \lambda_r}{\partial n_{\text{eff}}} \frac{\text{nm}}{\text{RIU}}. \quad (2)$$

The efficiency of this sensor is calculated by device sensitivity  $S_d$  for novel gradient strip-slot waveguide:

$$S_d = \frac{\partial \lambda_r}{\partial n_c} \frac{\text{nm}}{\text{RIU}}. \quad (3)$$

We analyzed this waveguide sensor at  $\lambda_0 = 1550$  nm. To validate this sensor sensitivity with other different wavelengths, the following equation is used to calculate normalized sensitivity  $S_d''$ :

$$S_d'' = \frac{S_d}{\lambda_0} (\text{RIU}^{-1}). \quad (4)$$

### 3. Results and Discussion

In the silicon photonic waveguide biosensor, evanescent wave interacts with analytes surrounding the core. Transverse electric mode is irregular at sidewalls, so the intensity of light waves will be maximum at the top of the waveguide structure. In this proposed design, we analyzed rib and gradient step rib-slot waveguide to get more interaction with samples over the length of 8 mm [34, 35]. The rib waveguide structure is more suitable for biosensing applications. The

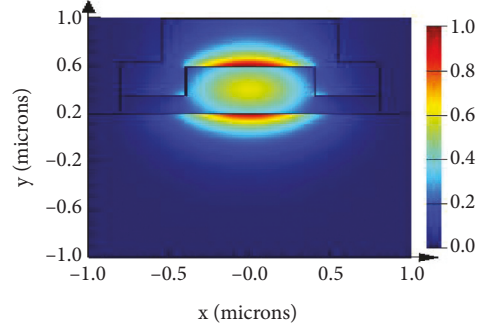


FIGURE 2: Rib waveguide with analyte.

transverse-electric (TE) polarization mode in the rib structure exhibits good performance over the waveguide for high index-contrast. TE mode exploits light vertically, so the analyte interaction with the waveguide has improved the bulk sensitivity. In the strip waveguide, the analyte interaction is only with the horizontal surface area. The field effect in the bottom layer comprising silicon oxide has no effect on sensitivity. At 1550 nm, the well-established CMOS foundry waveguide with a geometric width of 970 nm and height of 400 nm is used. In the proposed waveguide structure, transverse-electric field that exceeds 450 nm from the surface core provides higher sensitivity than TM [15]. This gradient-step waveguide structure helps to avoid antibody diffusion on the surface. By analysing such advantages, the proposed waveguide with 970 nm width is appropriately chosen. To obtain higher bulk sensitivity, the analyte thickness is optimized.

**3.1. Analyte Transporting for Bulk Sensitivity.** The biosensor uses biological analyte placed in sensing arm where the analyte interacts with the evanescent field, which is above the core. The analyte is a biomolecule that is minimal in its concentration, so the viscosity and density of the sample are not changed. Normally, the human C-reactive protein (CRP) molecule weight is 115 kilodalton. The analyte is placed in sensing arm to obtain bulk sensitivity of the photonic waveguide sensor. The concentration of the analyte at waveguide surface  $[A]_{\text{surface}}$  involves the variations of thickness and reaction of TE mode, which exceeds the waveguide surface  $[A](x, y, t)$ .

The temporal and spatial variations of the analyte in the sensing arm are described by the following diffusion equation:

$$\frac{\partial [A]}{\partial t} + u \frac{\partial [A]}{\partial x} + v \frac{\partial [A]}{\partial y} = D \left( \frac{\partial^2 [A]}{\partial x^2} + \frac{\partial^2 [A]}{\partial y^2} \right) + G, \quad (5)$$

where  $[A]$  is the analyte concentration in bulk,  $D$  is the diffusion coefficient of the analyte, and  $G$  denotes the reaction of the biomolecule in the waveguide surface [23]. The bulk sensitivity of the biosensor was analysed for four different analyte thicknesses, viz., 400 nm, 250 nm, 150 nm, and 90 nm, in the waveguide. In the rib and rib-slot waveguide structure, the effective index of each analyte thickness of the different samples is analyzed through FDTD [23]. Based on

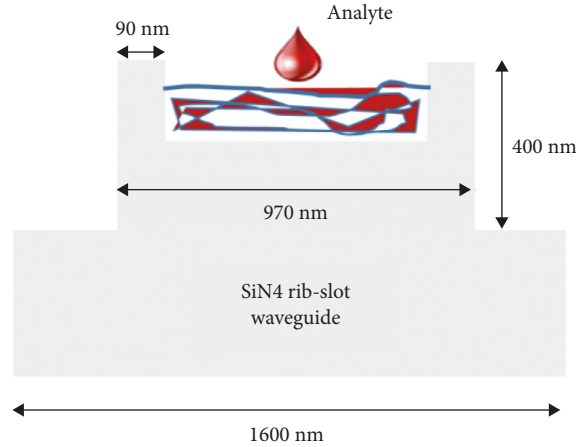
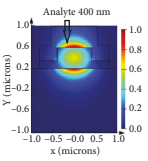
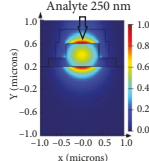
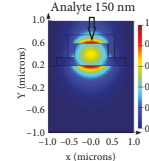
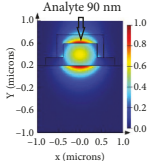


FIGURE 3: Novel gradient step rib-slot waveguide with analyte.

TABLE 1: Refractive index of different cancer cells [32].

| Name of the cell | Disease         | Refractive index |
|------------------|-----------------|------------------|
| Normal           |                 | 1.35             |
| Jurkat           | Leukemia        | 1.39             |
| HeLa             | Cervical cancer | 1.392            |
| PC-12            | Brain           | 1.395            |
| MDA-MB-231       | Breast cancer   | 1.399            |
| MCF-7            | Breast cancer   | 1.401            |

TABLE 2: Analysis of rib waveguide bulk sensitivity with the analyte thickness of 400 nm to 90 nm.

| RI         | 400 nm waveguide bulk sensitivity   | 250 nm waveguide bulk sensitivity   | 150 nm waveguide bulk sensitivity  | 90 nm waveguide bulk sensitivity   |
|------------|---|---|--|--|
| 1.35–1.401 | 0.3117 RIU/RIU<br> | 0.2501 RIU/RIU<br> | 0.1882 RIU/RIU<br> | 0.12764 RIU/RIU<br> |

the various analyte thickness, the rib and rib-slot waveguides for normal and cancer cell are measured at 1550 nm. Lumerical INTERCONNECT has foundry-specific PDK, which verifies the fabrication feasibility of this sensor. Figure 1 shows the silicon nitride biosensor setup. MZI rib waveguide sensor and novel gradient step rib-slot waveguide sensor are shown in Figures 2 and 3, respectively.

The optimized waveguide geometry of the rib structure is 400 nm thick, and 970 nm width is analyzed for sensitivity, applying bulk solution as analyte thickness. For bulk sensitivity calculation, the refractive index of the analyte normal cell is 1.35 and of the cancer cells varies from 1.39 to 1.401, as shown in Table 1. In this process, the effective index of each thickness is calculated.

FDTD analysis of the rib waveguide with analyte thickness of 400 nm, 250 nm, 150 nm, and 90 nm was carried out. Based on the effective index, using equations (1) and (3), the bulk sensitivity for different refractive indices was

computed, and the results are provided in Table 2. In this physical environment, the sensor is analysed with integration of all analyte thickness in the MZI sensing arm with a total length of 8mm. The density and viscosity of the analyte are not constant in the sensor physically. Based on these environmental factors, to improve the sensor sensitivity, the analyte thickness ranging from 400 nm to 90 nm with each thickness of the sensing arm with a length of 2 mm is analyzed.

The peak of the transmission spectrum of the rib waveguide, as shown in Figure 4, for the sample refractive index of 1.35 (normal cells) and 1.401 (cancer cells) is observed at 1563 nm wavelength. This shift in the transmission spectrum makes the sensor detect Breast Cancer (MCF-7). However, this rib waveguide structure is insensitive at 1563 nm over the normal cells. Due to this, the sensor detects cancer cells with minor variations in the transmission spectrum.

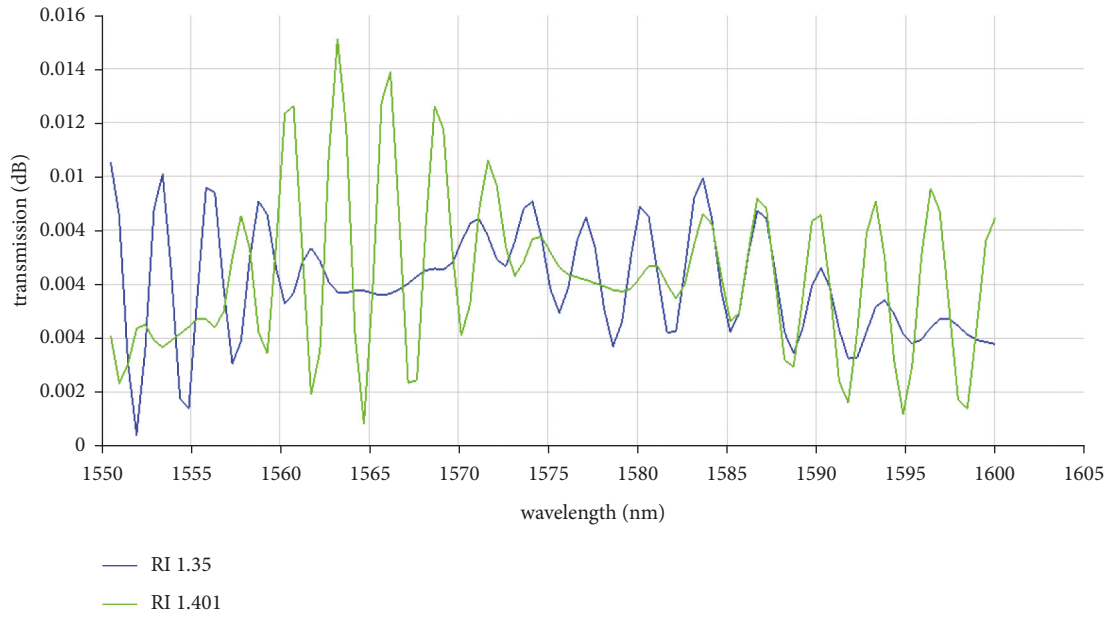


FIGURE 4: Transmission spectrum of normal cells with refractive index 1.35 vs Breast Cancer (MCF-7) cells with refractive index 1.401 of rib waveguide with integrated analyte thickness of 400 nm, 250 nm, 150 nm, and 90 nm.

TABLE 3: Analysis of bulk sensitivity of the rib-slot waveguide with 400 nm analyte thickness.

| RI    | Effective index | Effective area | 400 nm bulk sensitivity |
|-------|-----------------|----------------|-------------------------|
| 1.35  | 1.469133        | 1.53003        | 0.2574 (RIU/RIU)        |
| 1.39  | 1.479298        | 1.47212        |                         |
| 1.392 | 1.479832        | 1.46935        |                         |
| 1.395 | 1.480636        | 1.46522        |                         |
| 1.399 | 1.481717        | 1.45975        |                         |
| 1.401 | 1.482261        | 1.45703        |                         |

The field distribution plot shows the intensity of the light in the waveguide core and the 400 nm analyte layer. The x and y axes are in microns, ranging from -1.0 to 1.0. A color scale on the right indicates intensity from 0.0 to 1.0. The plot shows a strong field in the core and a smaller field in the analyte layer.

TABLE 4: Analysis of bulk sensitivity of rib-slot waveguide with 250 nm analyte thickness.

| RI    | Effective index | Effective area | 250 nm bulk sensitivity |
|-------|-----------------|----------------|-------------------------|
| 1.35  | 1.515538        | 1.26747        | 0.2033 (RIU/RIU)        |
| 1.39  | 1.523636        | 1.24779        |                         |
| 1.392 | 1.52405         | 1.24683        |                         |
| 1.395 | 1.524673        | 1.24538        |                         |
| 1.399 | 1.525507        | 1.24346        |                         |
| 1.401 | 1.525925        | 1.2425         |                         |

The field distribution plot shows the intensity of the light in the waveguide core and the 250 nm analyte layer. The x and y axes are in microns, ranging from -1.0 to 1.0. A color scale on the right indicates intensity from 0.0 to 1.0. The plot shows a strong field in the core and a smaller field in the analyte layer.

TABLE 5: Analysis of bulk sensitivity of rib-slot waveguide with 150 nm analyte thickness.

| RI    | Effective index | Effective area | 150 nm bulk sensitivity |
|-------|-----------------|----------------|-------------------------|
| 1.35  | 1.549438        | 1.16119        | 0.1333 (RIU/RIU)        |
| 1.39  | 1.555138        | 1.15424        |                         |
| 1.392 | 1.555426        | 1.15388        |                         |
| 1.395 | 1.555857        | 1.15334        |                         |
| 1.399 | 1.556433        | 1.15261        |                         |
| 1.401 | 1.556721        | 1.15225        |                         |

The field distribution plot shows the intensity of the light in the waveguide core and the 150 nm analyte layer. The x and y axes are in microns, ranging from -1.0 to 1.0. A color scale on the right indicates intensity from 0.0 to 1.0. The plot shows a strong field in the core and a smaller field in the analyte layer.

TABLE 6: Analysis of bulk sensitivity of rib-slot waveguide with 90 nm analyte thickness.

| RI    | Effective index | Effective area | 90 nm bulk sensitivity |
|-------|-----------------|----------------|------------------------|
| 1.35  | 1.569833        | 1.11425        | 0.0960 (RIU/RIU)       |
| 1.39  | 1.573702        | 1.11248        |                        |
| 1.392 | 1.573895        | 1.11236        |                        |
| 1.395 | 1.574184        | 1.11219        |                        |
| 1.399 | 1.574569        | 1.11195        |                        |
| 1.401 | 1.574761        | 1.11182        |                        |

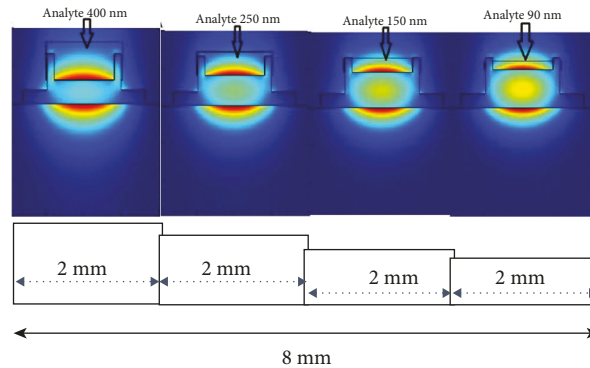
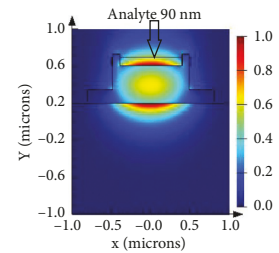


FIGURE 5: Gradient rib-slot waveguide structure with a width of 450 nm and height of 220 nm with integrated analyte thickness of 400 nm, 250 nm, 150 nm, and 90 nm.

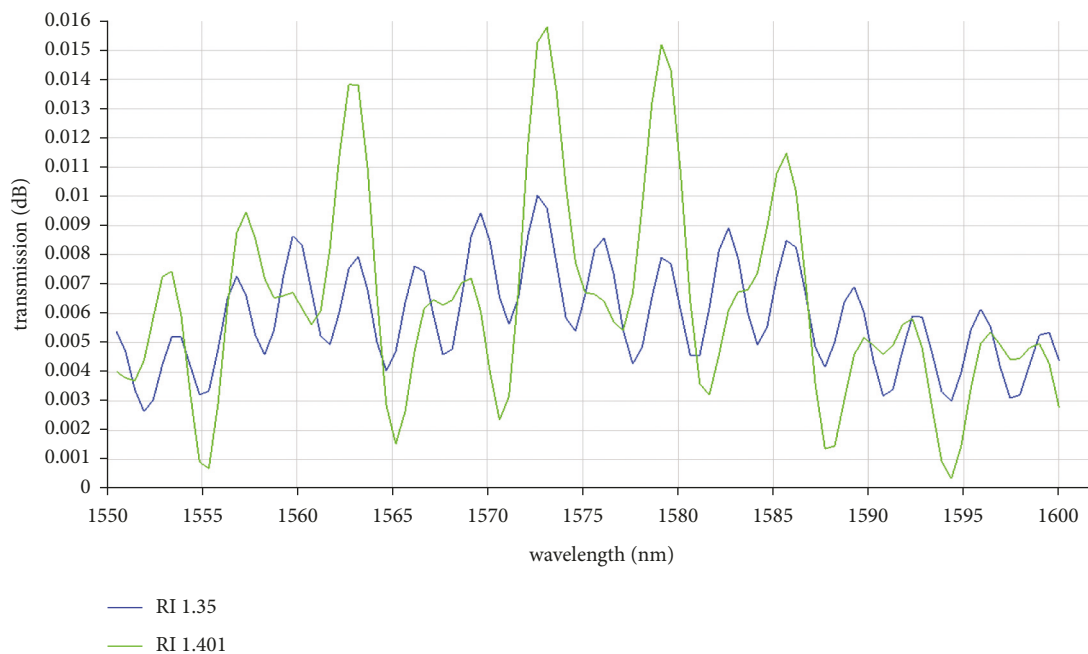


FIGURE 6: Silicon nitride rib-slot waveguide transmission spectrum of normal cells with refractive index 1.35 vs. Breast Cancer (MCF-7) cells with refractive index of 1.401 with integrated analyte thickness of 400 nm, 250 nm, 150 nm, and 90 nm.

**3.2. Novel Gradient Step Rib-Slot Waveguide.** This rib-slot waveguide with analyte is shown in Figure 3, a sensitive and enhanced guiding structure that provides a better confinement factor. Integration of the sample holder to the sensor is complex in fabrication over the small region. This proposed gradient step rib-slot waveguide holds the sample effectively

without any polydimethylsiloxane (PDMS) layer. Numerically, for different analyte thickness layers, the effective area was computed for 400 nm, 250 nm, 150 nm, and 90 nm; they are tabulated in Tables 3, 4, 5, and 6, respectively, with waveguide bulk sensitivity using equation (1) and sensor architecture sensitivity using equation (2). The theoretical

TABLE 7: Comparison of bulk sensitivity of  $\lambda_0 = 1550$  nm with other silicon-based photonic sensors.

| Sensor    | Architecture | $S_{w,bulk}$ (RIU/RIU) | $S_d$ (nm/RIU) | $S_d''$ (RIU <sup>-1</sup> ) |
|-----------|--------------|------------------------|----------------|------------------------------|
| [38]      | Ring         | 0.45                   | 383            | 0.247                        |
| [39]      | Ring         | 0.89                   | 490            | 0.316                        |
| [28]      | Ring         | 0.85                   | 440            | 0.284                        |
| [40]      | Ring         | 0.80                   | 580            | 0.374                        |
| [41]      | PSBG         | n/a                    | 579            | 0.374                        |
| [42]      | Ring         | 0.97                   | 575            | 0.371                        |
| [43]      | Ring         | 1.03                   | 545            | 0.352                        |
| [33]      | Bragg        | 0.93                   | 507            | 0.387                        |
| [44]      | MZI          | 0.79                   | -599           | -0.386                       |
| This work | MZI          | <b>2.0699</b>          | <b>568</b>     | <b>0.366</b>                 |

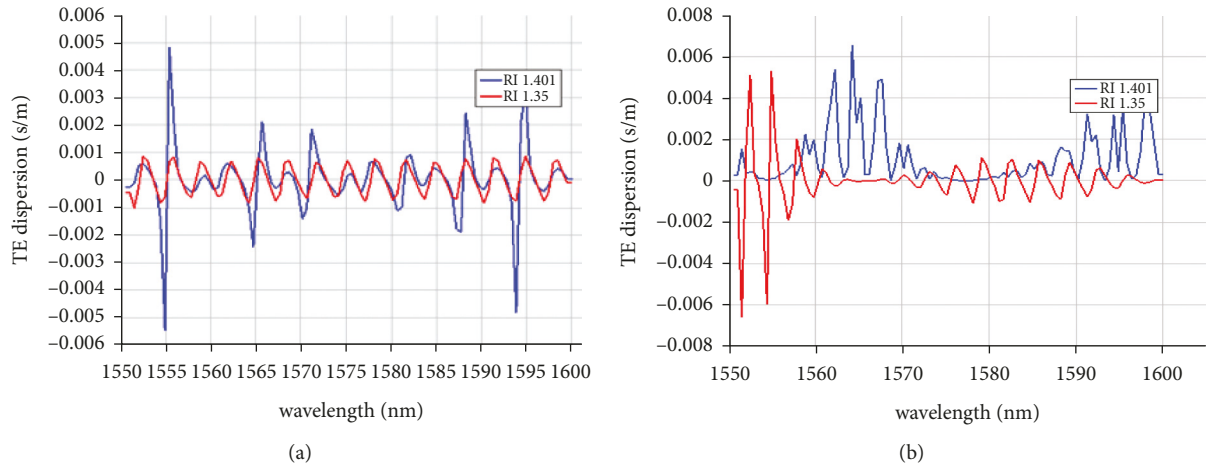


FIGURE 7: Dispersion of RI 1.35 normal cells and 1.401 cancer cells: (a) rib waveguide and (b) rib-slot waveguide.

analysis has been investigated considering the fabrication tolerance of the waveguide structure. The key task of waveguide optimization for bulk sensitivity is mode field distribution over the sensor surface. Analysis of the bulk sensitivity in the rib-slot waveguide, slot geometry of the 790 nm width, and 400 nm thickness with low index region that influences the analyte perfectly [36]. The gap region of the rib-slot guiding structure highly supports the TE mode, which gives evanescent waves to interact with the analyte in the highly effective area [31]. Thus, the waveguide guiding structure strongly influences the bulk sensitivity of this gradient step rib-slot biosensor. By integrating this in the Mach-Zehnder interferometer, the design of silicon photonics label-free biosensing for point-of-care devices will be more effective, and fabrication tolerance will be less compared to conventional waveguide structures like strip and slot waveguides.

By increasing the effective surface area in the sensor, the sample interacts more efficiently to obtain high waveguide bulk sensitivity. This numerical analysis of 400 nm, 250 nm, 150 nm, and 90 nm thickness in FDTD has been carried out based on device operation in the physical environment. Integration of all analyte thicknesses in the MZI sensing arm with a total length of 8  $\mu\text{m}$  generates increased absorption at three different wavelengths in the transmission spectrum, as shown in Figure 5. This proposed rib-slot waveguide

geometry optimization increases the detection rate of cancer cells compared with single analyte thickness of sensing arm length two  $\mu\text{m}$  waveguide.

The transmission spectrum of the rib-slot waveguide in Figure 6 shows the peaks at three different points of wavelength, 1563 nm, 1573 nm, and 1579 nm, of the sensor to detect Breast Cancer (MCF-7) cells. However, the rib-slot waveguide structure provides a good response and differentiates the cancer cells from the normal human cells. From the numerical analysis of different geometric, the proposed design of novel gradient rib-slot waveguide structure is in high bulk sensitivity. With 90 nm analyte thickness, in Table 7, the bulk sensitivity of breast cancer cells (MCF-7) is 1.1240 (RIU/RIU), which is higher than that in the rib waveguide. This structure makes the sensor efficient in detecting cancer cells. This design can be integrated in a point-of-care sensor system with a read-out.

The performance of the sensor depends upon the TE polarization on waveguide mode, as this analyte thickness is more sensitive to refractive index changes in cladding. In this numerical analysis, two different waveguide geometry structures, rib and rib-slot, have been simulated and the dispersion characteristics are studied [37]. In convention, silicon nitride waveguides achieve sharp bending with low loss, as shown in Figure 7(b), dispersion due to modes that overlap with the analyte. Rib-slot waveguide is more

dispersive than rib waveguide, as shown in Figure 7(a). However, the sensitivity of the rib-slot waveguide sensor is higher. Normalized sensitivity  $S_d''$  will be calculated to compare ( $\lambda_0$ ) for different wavelengths using equation (4).

#### 4. Conclusion

We proposed silicon nitride MZI sensor architecture as integrated biosensor for point-of-care device. This biosensor detects virus and biomolecules fast and is cost-effective. Our simulated analysis determines optimized waveguide geometry that maximizes the bulk sensitivity. MZI utilizes the refractive index of different cancer cells (1.39–1.401) to determine the waveguide bulk sensitivity ( $S_{w,bulk}$ ). In addition, we compared gradient step rib waveguide with rib-slot waveguide. The results show that the gradient step rib-slot waveguide is efficient and can hold analytes without any PDMS material. Analyte transportation and leakage of molecules at the edge of the waveguide lead to decrease in the sensitivity of the sensor. Our proposed design exhibits a high ( $S_{w,bulk}$ ) of 2.0699 RIU/RIU and a device sensitivity ( $S_d$ ) of 568 nm/RIU calculated based on analyte thickness. The absorption of cancer cells at three wavelengths 1563 nm, 1573 nm, and 1579 nm offers high detection rate compared with the standard rib waveguide. The silicon nitride-based waveguide biosensor may be fabricated using CMOS E-beam lithography, and its stability will be matched to the simulated results. The proposed biosensor can provide test results in a short time than the conventional biopsy, which takes two days to detect cancer cells.

#### Data Availability

The data underlying the results presented in this paper are not publicly available at this time but may be obtained from the authors upon reasonable request.

#### Conflicts of Interest

The authors declare that there are no conflicts of interest.

#### Authors' Contributions

Design and simulation analysis were performed by Prasanna Kumar. The manuscript preparation was performed by Prasanna Kumar and Sivasubramanian.

#### Acknowledgments

This proposed work was performed in the Fiber Optics Laboratory on Lumerical software provided by Vellore Institute of Technology, Chennai.

#### References

- [1] N. Bhalla, Y. Pan, Z. Yang, and A. F. Payam, "Opportunities and challenges for biosensors and nanoscale Analytical tools for pandemics: COVID-19," *ACS Nano*, vol. 14, no. 7, pp. 7783–7807, Jul. 2020.
- [2] "The global challenge of cancer," *Naturaliste Canadien*, vol. 1, no. 1, pp. 1-2, 2020.
- [3] H. Sung, J. Ferlay, R. L. Siegel et al., "Global cancer statistics 2020: GLOBOCAN estimates of incidence and mortality worldwide for 36 cancers in 185 countries," *CA: A Cancer Journal for Clinicians*, vol. 71, no. 3, pp. 209–249, 2021.
- [4] B. Hayes, C. Murphy, A. Crawley, and R. O'Kennedy, "Developments in point-of-care diagnostic Technology for cancer detection," *Diagnostics*, vol. 8, no. 2, p. 39, 2018.
- [5] S. Parra, E. Carranza, J. Coole et al., "Development of low-cost point-of-care technologies for cervical cancer prevention based on a single-board computer," *IEEE Journal of Translational Engineering in Health and Medicine*, vol. 8, pp. 1–10, 2020.
- [6] S. Schultz, D. R. Smith, J. J. Mock, and D. A. Schultz, "Single-target molecule detection with nonbleaching multicolor optical immunolabels," in *Proceedings of the National Academy of Sciences*, vol. 97, no. 3, pp. 996–1001, California, CA, USA, February 2000.
- [7] A. Cassidy, A. Parle-McDermott, and R. O'Kennedy, "Virus detection: a review of the current and emerging molecular and immunological methods," *Frontiers in Molecular Biosciences*, vol. 8, 2021.
- [8] V. Naresh and N. Lee, "A review on biosensors and recent development of nanostructured materials-enabled biosensors," *Sensors*, vol. 21, no. 4, p. 1109, 2021.
- [9] Y. Du, H. Wang, W. Cui et al., "Foodborne disease risk prediction using multigraph structural long short-term memory networks: algorithm design and validation study," *JMIR Medical Informatics*, vol. 9, no. 8, Article ID e29433, 2021.
- [10] F. Deeba, S. Kun, F. Ali Dharejo, and Y. Zhou, "Sparse representation based computed tomography images reconstruction by coupled dictionary learning algorithm," *IET Image Processing*, vol. 14, no. 11, pp. 2365–2375, 2020.
- [11] C. Chen and J. Wang, "Optical biosensors: an exhaustive and comprehensive review," *Analyst*, vol. 145, no. 5, pp. 1605–1628, 2020.
- [12] J. Yoon, M. Shin, T. Lee, and J.-W. Choi, "Highly sensitive biosensors based on biomolecules and functional nanomaterials depending on the types of nanomaterials: a perspective review," *Materials*, vol. 13, no. 2, p. 299, 2020.
- [13] Y. Liu, Q. Liu, S. Chen, F. Cheng, H. Wang, and W. Peng, "Surface plasmon resonance biosensor based on smart phone platforms," *Scientific Reports*, vol. 5, no. 1, Article ID 12864, 2015.
- [14] D. Thomson, A. Zilkie, J. E. Bowers et al., "Roadmap on silicon photonics," *Journal of Optics*, vol. 18, no. 7, 2016.
- [15] J. Milvich, D. Kohler, W. Freude, and C. Koos, "Surface sensing with integrated optical waveguides: a design guideline," *Optics Express*, vol. 26, no. 16, Article ID 19885, 2018.
- [16] L. Ali, M. U. Mohammed, M. Khan, A. H. B. Yousuf, and M. H. Chowdhury, "High-quality optical ring resonator-based biosensor for cancer detection," *IEEE Sensors Journal*, vol. 20, no. 4, pp. 1867–1875, 2020.
- [17] A. Densmore, E. Post, D.-X. Xu et al., "A silicon-on-insulator photonic wire based evanescent field sensor," *IEEE Photonics Technology Letters*, vol. 18, no. 23, pp. 2520–2522, 2006.
- [18] R. Baets, A. Z. Subramanian, S. Clemmen et al., "Silicon photonics: silicon nitride versus silicon-on-insulator," in *Proceedings of the Optical Fiber Communication Conference*, Washington D.C., USA, 2016.
- [19] D. J. Blumenthal, R. Heideman, D. Geuzebroek, A. Leinse, and C. Roeloffzen, "Silicon nitride in silicon photonics," in *Proceedings of the IEEE*, vol. 106, no. 12, pp. 2209–2231, Piscataway, NJ, USA, December 2018.

- [20] Y. Xie, M. Zhang, and D. Dai, "Design rule of mach-zehnder interferometer sensors for ultra-high sensitivity," *Sensors*, vol. 20, no. 9, p. 2640, 2020.
- [21] A. Z. Subramanian, E. Ryckeboer, A. Dhakal et al., "Silicon and silicon nitride photonic circuits for spectroscopic sensing on-a-chip (Invited)," *Photonics Research*, vol. 3, no. 5, p. B47, 2015.
- [22] C. Chen, X. Hou, and J. Si, "Protein analysis by Mach-Zehnder interferometers with a hybrid plasmonic waveguide with nano-slots," *Optics Express*, vol. 25, no. 25, Article ID 31294, 2017.
- [23] M. Selmi, M. H. Gazzah, and H. Belmabrouk, "Optimization of microfluidic biosensor efficiency by means of fluid flow engineering," *Scientific Reports*, vol. 7, no. 1, p. 5721, 2017.
- [24] S. Prasanna Kumar and A. Sivasubramanian, "Optimization of silicon photonic strip waveguide for detection of diabetes mellitus," *Materials Today: Proceedings*, vol. 45, 2020.
- [25] P. Muñoz, G. Micó, L. Bru et al., "Silicon nitride photonic integration platforms for visible, near-infrared and mid-infrared applications," *Sensors*, vol. 17, no. 9, pp. 2088–2125, 2017.
- [26] R. R. Singh, S. Kumari, A. Gautam, and V. Priye, "Glucose sensing using slot waveguide-based SOI ring resonator," *IEEE Journal of Selected Topics in Quantum Electronics*, vol. 25, no. 1, pp. 1–8, 2019.
- [27] X. Sun, D. Dai, L. Thylén, and L. Wosinski, "High-sensitivity liquid refractive-index sensor based on a Mach-Zehnder interferometer with a double-slot hybrid plasmonic waveguide," *Optics Express*, vol. 23, no. 20, Article ID 25688, 2015.
- [28] H. Yan, L. Huang, X. Xu et al., "Unique surface sensing property and enhanced sensitivity in microring resonator biosensors based on subwavelength grating waveguides," *Optics Express*, vol. 24, no. 26, Article ID 29724, 2016.
- [29] J. Gonzalo Wangüemert-Pérez, P. Cheben, A. Ortega-Moñux et al., "Evanescent field waveguide sensing with sub-wavelength grating structures in silicon-on-insulator," *Optics Letters*, vol. 39, no. 15, p. 4442, 2014.
- [30] Q. Liu, X. Tu, K. W. Kim et al., "Highly sensitive Mach-Zehnder interferometer biosensor based on silicon nitride slot waveguide," *Sensors and Actuators B: Chemical*, vol. 188, pp. 681–688, 2013.
- [31] S. Prasanna Kumar and A. Sivasubramanian, "Optimization of the transverse electric photonic strip waveguide biosensor for detecting diabetes mellitus from bulk sensitivity," *Journal of Healthcare Engineering*, vol. 2021, Article ID 6081570, 8 pages, 2021.
- [32] X. J. Liang, A. Q. Liu, X. M. Zhang, P. H. Yap, T. C. Ayi, and H. S. Yoon, "Determination of refractive index for single living cell using integrated biochip," in *Proceedings of the 13th International Conference on Solid-State Sensors, Actuators and Microsystems, 2005. Digest of Technical Papers. TRANSDUCERS'05*, vol. 2, pp. 1712–1715, Seoul, Korea (South), June 2005.
- [33] C. Pérez-Armenta, A. Ortega-Moñux, J. Čtyroký et al., "Narrowband Bragg filters based on subwavelength grating waveguides for silicon photonic sensing," *Optics Express*, vol. 28, no. 25, Article ID 37971, 2020.
- [34] V. R. Almeida, Q. Xu, C. A. Barrios, and M. Lipson, "Guiding and confining light in void nanostructure," *Optics Letters*, vol. 29, no. 11, p. 1209, 2004.
- [35] T. Claes, J. G. Molera, K. De Vos, E. Schacht, R. Baets, and P. Bienstman, "Label-free biosensing with a slot-waveguide-based ring resonator in silicon on insulator," *IEEE Photonics Journal*, vol. 1, no. 3, pp. 197–204, 2009.
- [36] A. Habibzadeh-Sharif and M. Soleimani, "Rib-based slot waveguide for nonlinear silicon photonics," in *Proceedings of the 20th Iranian Conference on Electrical Engineering*, pp. 55–60, Tehran, Iran, May 2012.
- [37] S. Chandran, R. K. Gupta, and B. K. Das, "Dispersion enhanced critically coupled ring resonator for wide range refractive index sensing," *IEEE Journal of Selected Topics in Quantum Electronics*, vol. 23, no. 2, pp. 424–432, 2017.
- [38] V. Donzella, A. Sherwali, J. Flueckiger, S. M. Grist, S. T. Fard, and L. Chrostowski, "Design and fabrication of SOI microring resonators based on sub-wavelength grating waveguides," *Optics Express*, vol. 23, no. 4, p. 4791, 2015.
- [39] J. Flueckiger, S. Schmidt, V. Donzella et al., "Sub-wavelength grating for enhanced ring resonator biosensor," *Optics Express*, vol. 24, no. 14, Article ID 15672, 2016.
- [40] E. Luan, H. Yun, L. Laplatine et al., "Enhanced sensitivity of subwavelength multibox waveguide microring resonator label-free biosensors," *IEEE Journal of Selected Topics in Quantum Electronics*, vol. 25, no. 3, pp. 1–11, 2019.
- [41] E. Luan, H. Yun, M. Ma, D. M. Ratner, K. C. Cheung, and L. Chrostowski, "Label-free biosensing with a multi-box sub-wavelength phase-shifted bragg grating waveguide," *Bio-medical Optics Express*, vol. 10, no. 9, p. 4825, 2019.
- [42] E. Luan, K. M. Awan, K. C. Cheung, and L. Chrostowski, "High-performance sub-wavelength grating-based resonator sensors with substrate overetch," *Optics Letters*, vol. 44, no. 24, p. 5981, 2019.
- [43] C.-W. Chang, X. Xu, S. Chakravarty et al., "Pedestal sub-wavelength grating metamaterial waveguide ring resonator for ultra-sensitive label-free biosensing," *Biosensors and Bioelectronics*, vol. 141, Article ID 111396, 2019.
- [44] M. Odeh, K. Twayana, K. Sloyan, J. E. Villegas, S. Chandran, and M. S. Dahlem, "Mode sensitivity analysis of sub-wavelength grating slot waveguides," *IEEE Photonics Journal*, vol. 11, no. 5, pp. 1–10, 2019.